ICME2015

International Conference on Mechanical Engineering 2015
(ICME 2015) 18 – 20 December, 2015, Dhaka, Bangladesh

Paper ID : 352

CFD Study of Detailed Flow Field and Performance of Swirling Savonius Wind Turbine

Abdullah Al-Faruk[1, 2, a)], Ahmad Sharifian[2, b)] and Andrew P. Wandel[2, c)]

[1]*Department of Mechanical Engineering, Khulna University of Engineering & Technology*
Khulna 9203, Bangladesh
[2]*Computational Engineering and Science Research Centre, University of Southern Queensland*
Toowoomba 4350, Australia

a)Corresponding author: alfaruk.bd@gmail.com, U1031944@usq.edu.au
b)sharifia@usq.edu.au
c)andrew.wandel@usq.edu.au

Abstract. A novel hybrid wind turbine (Swirling Savonius, SST) that combines the conventional Savonius turbine and the split channel capable of inducing swirling flow has been suggested. Previous works indicate a performance improvement in the SST compared to the conventional Savonius turbine. However, the lack of detailed descriptions of the flow field around the SST inhibits complete understanding of performance of the hybrid turbine. The aim of this study is to numerically explore the 3D unsteady flow field around the rotor, and develop a dynamic simulation method for predicting the aerodynamic coefficients using ANSYS-CFX. Simulations results were compared with the experimental results with a good accuracy. A discussion on the detailed flow field characteristics, including velocity vector, velocity streamlines, pressure distribution, vorticity analysis, and examination of power and torque coefficients behavior are presented.

INTRODUCTION

Wind power has now firmly established itself as the mainstream electrical generation option with the least cost when adding new capacity to the grid, and the price continues to fall [1]. Greenpeace predicted that wind power could reach nearly 2000 GW by 2030 supplying 16.7% to 18.8% of global electricity, helping save over 3 billion tons of CO2 emissions annually [1]. Solar energy, on the other hand, covers a minor portion of global energy demands and generates less than 1% of the total electricity supply [2]. This is due to solar power being considered the most expensive type of renewable energy, although renewable sources may serve the best solution for decentralized energy supply for remote communities [3, 4]. However, the main challenge for stand-alone applications in remote regions is that the renewable energy sources are dependent on unpredictable factors such as weather and climatic conditions and may not match the load demand. The complementary nature of solar and wind energy can overcome the weaknesses of one through the strengths of the other. The hybrid renewable power generation with energy storage device may render the renewable energy sources more reliable and affordable means of generating electricity.

Among the wind turbines, Savonius wind turbine has many advantages over others such as simplicity in construction, self-starting and operating capability at low wind speed, and better visibility to animals, and free from harmful low frequency noise [5]. The Savonius turbines are popular for ventilation and pumping applications, but not employed for large scale power production projects because of low power coefficient (17% maximum) and slow running behavior [6]. Improving the power coefficient of the Savonius turbine can pave the way for using it for the local generation of electricity in rural environments where power is crucial for human development.

An innovative technique of performance improvement was proposed by combining the split channel mechanism with the primary Savonius wind turbine mechanism to a new hybrid design of Swirling Savonius turbine (SST) [7]. They proposed the hot air sourced from either solar thermal system or industrial waste heat as the heat source for the split channel. Split channels are capable of inducing swirling flow using hot air plume at the bottom of the channel

[8]. An increase in rotational speed and power coefficient of the SST compared to conventional Savonius turbine was reported [7]. Experimentally investigation on the geometrical parameters of the SST rotor confirmed a 25.5% increase in power coefficient compared to the optimum conventional Savonius turbine [5]. The SST rotor consists of two identical blades which are moved sideways and overlap like the conventional Savonius turbine as shown in Fig. 1. Unlike the conventional rotor of 180º blade arc angle, the inner tips of the blades extend further to construct the split channel which accommodate inside the turbine geometry [5]. A bottom hole acts as the hot air inlet of the swirling chamber, whereas, the top end plate provides an opening to the chamber.

FIGURE 1. Schematic diagrams of (a) conventional and (b) Swirling Savonius turbines

The lack of detailed descriptions of the flow field around the SST prevents complete understanding of working behavior of the turbine. To understand the combined mechanism of the hybrid rotor, a discussion on the detailed flow field characteristics, including the velocity vectors, velocity streamlines, pressure and temperature distributions, and vorticity analysis in the swirling chamber are required. In the present study, a computational fluid dynamics (CFD) model is developed using the finite volume based package of ANSYS-CFX 14.5 to explore the 3D unsteady flow pattern around the rotor, to understand the torque generation mechanism, and to analyze the performance of the hybrid turbine.

MODEL DEVELOPMENT

The geometry of SST rotor and the computational domains of the numerical modelling were developed using DesignModeler, a program of ANSYS Workbench. The rotor dimensions were chosen as the same as one of the experimental rotors which were 33.70 cm height and 31.05 cm diameter. The cylindrical domain had a diameter equivalent to 1.4 times of rotor diameter, so the diameter of the cylindrical rotating domain was 43.47 cm. The blades were 3 mm thick and the end plates were modelled as a circular disk of 4 mm thickness and diameter of 34.16 cm; 10% larger than the rotor diameter. The rotor aspect ratio, blade arc angle, and blade overlap ratio were 1.08, 195° and 0.25, respectively. The diameter of swirling chamber inlet and outlet were 25 mm and 100 mm, respectively.

To determine the domain size necessary to ensure that the boundary conditions had a minimal effect on the performance parameters, a series of domain size independence tests were performed. The dimensions of the computational domain were determined in multiples of the rotor diameter. Five different sized domains from five to fifteen times of rotor diameter (5×D to 15×D, see Fig. 2(a) for illustration) were simulated with the same numerical settings. The results showed that for the smallest domain (5×D; 155 cm cross-stream width by 233 cm stream wise length), a considerable increase in torque coefficient was observed. However, the change in the maximum torque coefficient between the 7.5×D domain and the 15×D domain is less than 5%. The height of the calculation domain was determined by the rotor height as illustrated by Fig. 2(b). The convergence study demonstrates that the distance of top boundary from rotor top has negligible effects. The maximum values of the torque coefficient vary around 2% ranging from the domain height of 1.5×H to 3×H with the 10×D domain.

ANSYS Meshing was used to discretize the computational domains which consist two parts: fixed and rotating. The sliding meshes were located in the circular region circumscribed by the interface as shown in Fig. 2. The rotating domain was constructed with an unstructured mesh to ensure a better adaption to the curved geometry of the blade

and to avoid directional effects as the circular domain rotates [9]. On the other hand, to ensure better organization and to reduce the effects of numerical diffusion, structured mesh was used in the fixed domain [10]. A highly refined mesh was applied in close proximity to the blades to improve the assessment of the boundary layer. The concentration of the cells at the interface between the rectangular and cylindrical regions was uniform and controlled by edge sizing with an equal number of divisions.

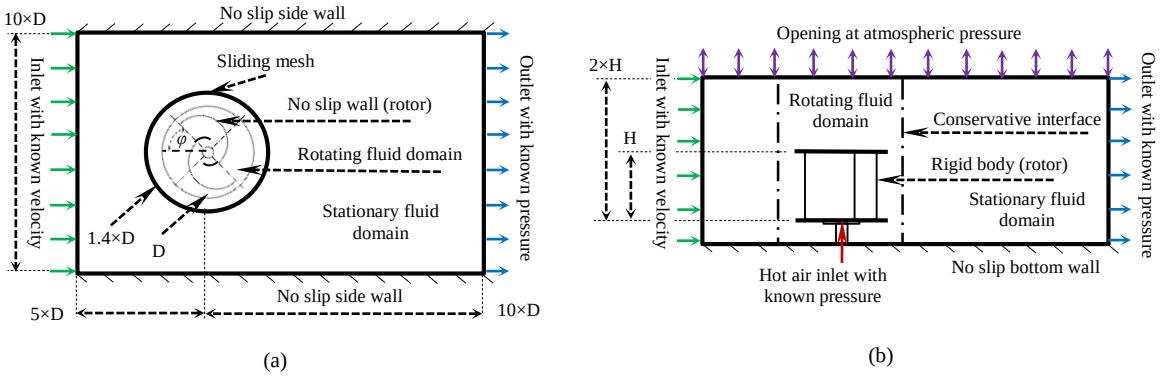

FIGURE 2. Boundary conditions of computational domain: (a) top view and (b) side view of the domain (rotor not to scale)

The number and distribution of nodal points within the flow domain dictates the accuracy of the final solution to a large degree. For this work, a family of hybrid grids was created in the hope of finding grid that provides adequate resolution of the unsteady phenomena while the methodology of the grid construction process remains the same in all meshes. The mesh quality was maintained by keeping the mesh metric (skewness) less than 0.83 in all the grids in the study. A very coarse mesh of 52,824 nodes to a much more refined mesh of 791,687 nodes were used in grid convergence study with 10×D, 2×H domain. The results showed that the coarsest mesh provides higher torque coefficients than the other meshes; most likely due to large mesh spacing near the walls and a breakdown of the conditions necessary to satisfy the turbulence model. However, for the remaining four finest meshes from 304,721 to 791,687 nodes, the torque coefficient varies by only around 5%.

The modelling used a transient approach with a fully implicit time advancement scheme. To ensure sufficient resolution of the numerical results an appropriate time-step size is required. A time-step independence study were conducted using the 10×D, 2×H domain with 791,689 nodes. The length of a time-step is inversely proportional to the rpm. Six different time-step sizes were simulated at 167 rpm corresponding to 25°, 10°, 5°, 2°, 1°, and 0.5° rotation per time-step of the inner cylindrical domain and the rotor. For the three largest time-steps, the rotor moves by rather substantial degrees resulting in a considerable change in the local body of fluid surrounding the blade. This causes over-predicting of the torque coefficients at the higher degrees of rotation per time-step. For the three smallest time-step sizes, the maximum torque coefficient varies by less than 2%.

A schematic of the computational domains including the boundary conditions is presented in Fig. 2. The inner cylindrical domain that contains the rotor rotates about the vertical axis with the same angular velocity as that of the rotor, whereas the outer rectangular domain is fixed. The interface between the rotating cylindrical domain and the stationary rectangular domain was handled by the sliding mesh feature. The fluid-fluid interfaces between the two mesh domains were set to conservative interface flux conditions [11, 12]. The conservative interface allows the mass and momentum, turbulence, and heat transfer quantities to flow between the boundaries on either side of the interface. At the inlet 5 m/s wind velocity was prescribed, while pressure was considered equivalent to atmospheric pressure at the outlet with zero relative static pressure and an unknown direction. All surfaces of the rotor were assumed to be smooth and adiabatic and were defined as no-slip wall boundary condition. The two sides of the computational domains as well as the bottom boundary were considered as no-slip adiabatic walls in accordance with the test bench surface in experimental study. However, the top boundary of the domain was defined as opening type as indicated by two way arrows in Fig. 2(b). The opening boundary condition allowed the fluid to cross the boundary surface in either direction. The hot air inlet at the bottom of the swirling chamber was defined as an inlet but treated differently. Instead of specifying the velocity, the total relative pressure was set at zero with 100ºC temperature was specified as the hot air flow was modelled as buoyancy driven.

The initial rotation of the rotor was set to each simulation by specifying the angular velocity of the region of sliding mesh about Y-axis. The rotor was treated as a rigid body that moves due to the fluid forces and torques acting upon

it. The structural deformations of the rotor were neglected but its kinematics was considered. Torques acting on the rigid body were the aerodynamic moment and the external brake torque added in the negative direction of rotor motion. The rotors were allowed to reach a steady state in response to the wind forces. Shear stress transport turbulence model was used in the simulations as it has been shown to perform well for highly separated aerodynamic flows [13]. Values for the turbulent quantities were specified indirectly by specifying the turbulence intensity (5%) and the eddy viscosity ratio in boundary conditions. The initial conditions were set to room temperature, room pressure and the initial velocities were defined as zero. The ambient temperature was assumed to be constant (25°C), but hydrostatic pressure change with height.

To validate the numerical model, the aerodynamic coefficients were compared with those of the experimental data. The size of the rotor and all the parameters in the numerical model were kept the same as the experimental conditions. The power coefficient against tip speed ratio plot for the experimental and the numerical simulations are presented in Fig. 3. The numerical model over predicting the power coefficients compared to the experimental data. The trend of the C_p curves are almost identical as shown in Fig. 3. The maximum power coefficient found in the SST turbulence model is around 24.5% at 0.71 tip speed ratio whereas it was 23.3% in the experiment. It can be concluded that a good agreement was found with only 4.7% error.

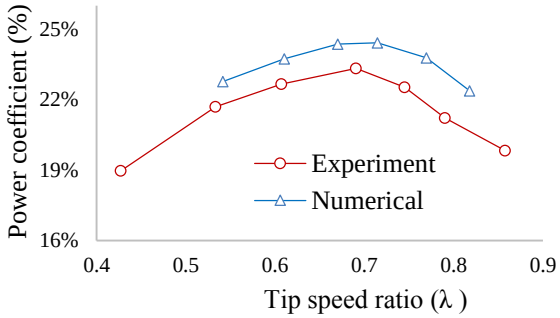

FIGURE 3. Comparison and validation of turbulence numerical models with wind tunnel experimental results of SST rotor

RESULTS AND DISCUSSION

Aerodynamic coefficients analysis

A set of dynamic simulations were performed to obtain the torque and power coefficient curves. The simulations were started at unique initial conditions of rotor angular velocity and external torque (load) applied to the negative direction of rotor motion. The time-steps in the simulations corresponded to 1° rotation per time-step. The initial angular velocities for the simulations were chosen in 10 intervals up to a maximum velocity which corresponded to a tip speed ratio of 1. The applied external torques were varied from 0.21 to 0.01 N.m. The time-steps were correspondingly varied between 0.006 and 0.0005 sec. The periodic steady state (mean value of sine curve) angular speed and torque values were used to analyze the aerodynamic performance of the rotors in terms of power and torque coefficients. The simulation outputs were averaged over two cycles at the periodic steady state condition. The averaged torque and power coefficients versus the tip speed ratio for the above dynamic simulations are presented at steady state conditions in Fig. 4. At higher applied torque, steady state angular velocity (tip speed ratio) is low so the power coefficient is lower as power is product of torque and angular speed. At lower external torque, while the angular velocity is high, lower torque and power coefficients are produced. However, power coefficients are higher at the mid regions of applied external torque. The maximum power coefficient of 20.60% was at 0.11 N.m load with a 0.66 the tip speed ratio.

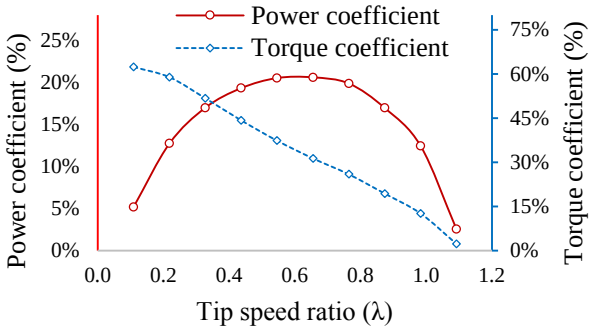

FIGURE 4. Dynamic power and torque coefficients versus blade tip speed ratio

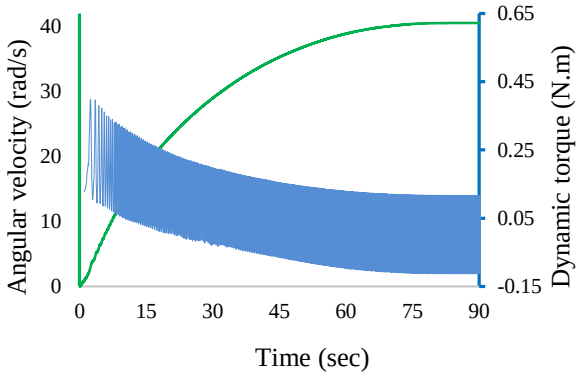

FIGURE 5. Time dependent angular velocity (left axis) and dynamic torque (right axis) with 0 rad/s initial angular velocity and 0 N.m load

The variation of angular velocity and rotor torque about the vertical axis as a function of physical simulation time at an initial condition of 0 rad/s angular velocity, 0 N.m external torque and 0.0005 sec time-step is shown in Fig. 5. The figure illustrates the evolution of angular velocity and torque from the initial conditions to the periodic steady state conditions. The curves of these two parameters stabilize at their periodic steady state condition at around 75 sec of simulation time. The average values of angular speed and rotor torque at the periodic steady state condition are 40.53 rad/s and 0 N.m, respectively.

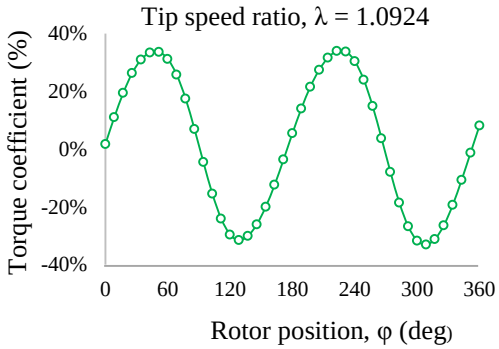

FIGURE 6. Torque coefficient versus angular position of rotor

The evolution of dynamic torque coefficients over one complete rotation of turbine at a periodic steady state is shown in Fig. 6. The tip speed ratio at this condition is 1.0924 without any applied load. The figure shows that the torque coefficient curve follows a sine curve with a large variation over one revolution of the rotor. Therefore, the mechanical power of the SST rotor fluctuates due to the wide variation of torque. Rotor torques are positive between 0° and 90° and again from 180° to 270°, and are negative for other positions of the rotor as illustrated by the azimuth angle in Fig. 2(a). The net torque without any external load at the periodic steady state condition is zero. The large fluctuation of torque mainly due the shape of the blades indicating all positions with respect to wind direction are not favorable in torque generation. Because of this large variation, analysis and comparison of power coefficient are difficult to comprehend. So the angular velocity and torque values were averaged over a few revolutions in periodic steady state to obtain the performance coefficients in the numerical study.

Flow field analysis

The flow field around the SST rotor blades and the swirling flow in the chamber was analyzed by the streamlines from the hot air inlet of the chamber. The streamlines of swirling flow colored by velocity from the hot air inlet is shown in Fig. 7 at 90° position of the rotor. The figure illustrates the generation of swirling flow inside the SST rotor. Hot air enters into the swirling chamber through the circular inlet at the bottom end plate by natural convection and

extracts the surrounding air through the slits of the chamber. The velocity of the entrained air formed the vortex with the hot air. The angular motion of the rotor provide the angular momentum to impart the swirling flow into the chamber. It has observed that the swirling flow is strong and reached the top end plate at 0° and 45° azimuth angles. However, at 90° and 135° positions of the rotor, the swirling flow decays along the height of the rotor and does not reach the top end plate. At the positions of stronger swirling flow, the power and torque coefficients are higher compared to the other positions.

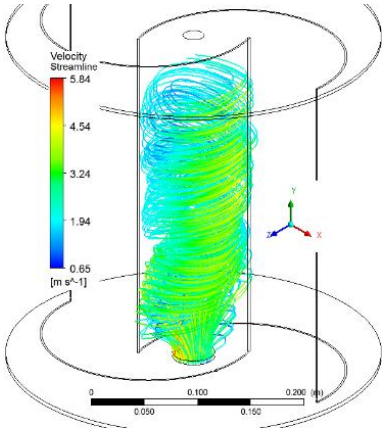

FIGURE 7. Velocity streamlines from hot air inlet at 90° position of rotor. Wind direction is negative Z-axis

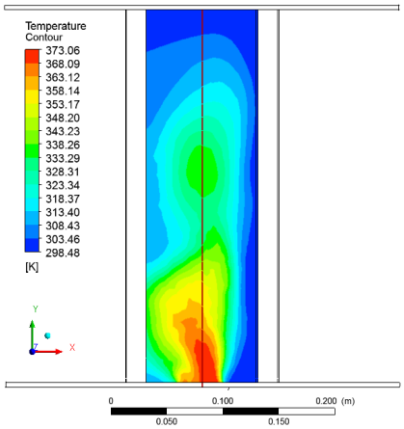

FIGURE 8. Temperature distribution in the swirling chamber in a perpendicular plane at 90° position. Wind direction is negative Z-axis

The distribution of hot air temperature in the swirling chamber has been analyzed through the temperature contours at different angular positions of the rotor. The contours showed that for the 0° and 45° positions, the hot air is more widespread compared to the 90° and 135° positions. Temperature is quickly reduced to free-stream wind temperature at the 135° position. This conclude that the hot air is not penetrating and a very good mixing is happening at this position. The contour illustrated in Fig. 8 are colored by temperature in an 8.30 cm×33.10 cm XY-plane at the central axis and 90° angular position of the rotor.

The strength of the swirling flow can be estimated by the velocity curl in the Y-direction which is the same as vorticity [14]. The velocity curl at Y-direction along the centerline of the rotor was taken from the CFD-Post tool of ANSYS using the velocity curl function. The average vorticity representing the swirling strength of the flow is shown in Fig. 9. The figure demonstrates that swirling strength is increasing with rotor height along the centerline and reached a maximum of around 120 s^{-1} at a 0.20 height ratio. This behavior is congruent with the streamline shown in Fig. 7. The average strength of the swirling flow is about 100 s^{-1}. Swirling strength at different positions revealed that it is higher at 0° and 45° positions than at 90° and 135° positions.

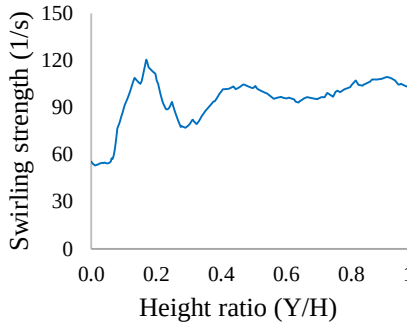

FIGURE 9. Swirling strength of flow along the centerline at 90° rotor position

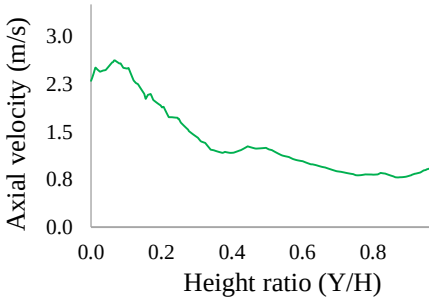

FIGURE 10. Axial velocity of hot air along the centerline at 90° rotor position

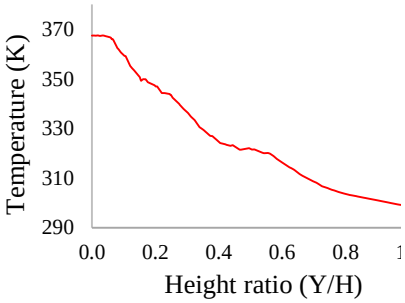

FIGURE 11. Axial temperature distribution of hot air along the centerline at 90° rotor position

FIGURE 10 presents the average axial velocity of the hot air for the four positions of the rotor along the centerline. The figure demonstrates that the velocity decreases along the centerline. At 0 height ratio, the velocity is around 2.5 m/s which is gradually reduced to around 1 m/s at a height ratio of 0.99 before reaching to zero at the top of the rotor. Figure 11 shows the variation of hot air temperatures along the centerline of the rotor. The temperature of hot air is gradually decreasing from inlet to free-stream temperatures. The decaying rate of hot air temperatures depends on the rotor position with the direction of wind and it is faster at 90° and 135° positions than the other two. The hot air temperature fell to free-stream temperature at a height ratio of 0.75 and 0.60 for 90° and 135° positions, respectively. On the other hand, the hot air temperatures gradually fell to ambient temperature at the top of the rotor for the 0° and 45° positions. This behavior is consistent with the fact that the relatively week swirling flows did not reach the top end plate for 90° and 135° positions because of the early decay of hot air temperatures. However for 0° and 45° positions, it did reach the top. These orientation allows quick sweeping of hot air might be the reason of faster decay of hot air temperature. The torque coefficient at first quarter (0° to 90°) are higher than the second quarter (90° to 180°) positions as seen in Fig. 6, is also aligned with the behavior.

The velocity vector fields at mid height of the rotor for 90° position is presented in Fig. 12. The normalized velocity vector is colored by the local velocities. The velocity vector along with the pressure contour (see Fig. 13) confirmed the generation of swirling flow in the chamber. It was observed that at 0°, 90°, and 135° positions, the vortices are formed through the entrainment of air from one slit, the wind strikes on the advancing blade and enters the chamber. However, for 45° position, wind enters through the both slits to form the vortex. Secondary vortices are also formed on the concave side of the returning blade at 0°, 90°, and 135° positions but that is not noticeable at the 45° angle. These vortices contribute to improving the performance of the SST rotor by increasing pressure on the concave side of the returning blade. The vortices creates anti-clockwise torque on the returning blade of the rotor which minimize the negative torque on the returning blade by the free-stream wind.

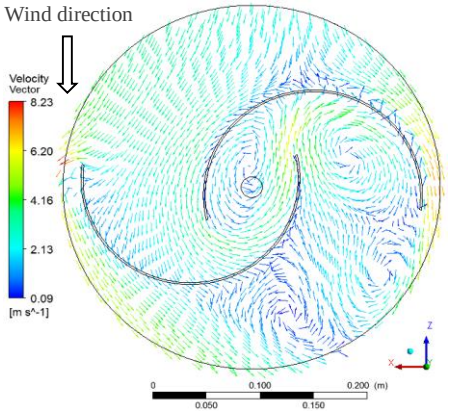

FIGURE 12. Velocity vectors at mid height and 90° position of rotor

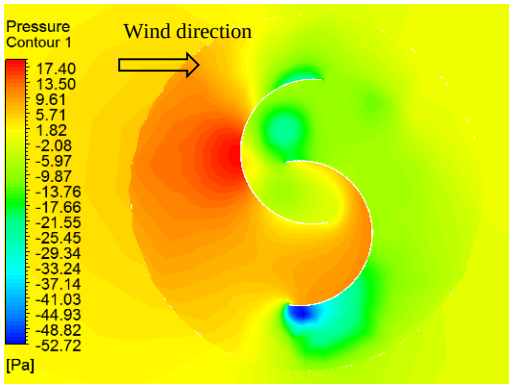

FIGURE 13. Pressure distribution around the SST rotor blades at mid height and 90° position of rotor

The pressure contours at 90° position presented in Fig. 13 can be used to describe the torque production mechanism of the SST rotor. The rotor torque is generated by drag forces due to the region of high pressure acting on the concave side of the advancing blade and the vortex generated in the swirling chamber. However, the region of high pressure acting on the convex side of the returning blade creates negative torque about the center of rotation. The re-circulation of air flow after striking the advancing blade to strike towards the concave side of the returning blade also contributes to the positive torque.

CONCLUSIONS

Numerical simulations were analyzed to gain a better understanding of the swirling flow behavior. Computational results were validated with the experimental results to be confident of the numerical results. The flow pattern and the velocity, pressure and temperature fields of the SST rotor were studied to understand the working behavior and torque generation mechanism. The streamlines and the velocity vectors at different angular positions of the rotor with respect to the direction, confirmed that swirling flows were generated inside the SST rotor. The average strength of the

swirling flows was around 95 s^{-1} and reached a maximum at 0.20 height ratio. The results showed that the torque as well as power of the SST varies largely depends on the azimuth angle of the rotor, and performance is better at 0° and 45° positions compared to 90° and 135°. The temperature and axial velocity of the inlet hot air reduces along the centerline of the rotor for all positions of the rotor.

REFERENCES

1. GWEC, *Global wind energy outlook*, (Greenpeace & Global Wind Energy Council, 2014).
2. K.H. Solangi, M.R. Islam, R. Saidur, N.A. Rahim and H. Fayaz, "A review on global solar energy policy," Renewable and Sustainable Energy Reviews, 15 (2011), pp. 2149–2163.
3. ESTIF, *Solar thermal markets in Europe*, (European Solar Thermal Industry Federation, Brussel, 2006).
4. A.M.O. Haruni, "A stand-alone hybrid power system with energy storage," Centre of Renewable Energy and Power Systems, (University of Tasmania, Tasmania, 2013).
5. A. Al-Faruk and A. Sharifian, "Influence of blade overlap and blade angle on the aerodynamic coefficients in vertical axis swirling type Savonius wind turbine," 19th Australasian Fluid Mechanics Conference, Melbourne, Australia, 2014.
6. M.A. Kamoji, S.V. Prabhu and S.B. Kedare, "Experimental investigations on the performance of conventional Savonius rotor under static and dynamic conditions," 3rd International Conference on Fluid Mechanics and Fluid Power, 2006.
7. A. Al-Faruk, A.S. Sharifian and S.R. Al-Atresh, "Numerical investigation of performance of a new type of Savonius turbine," 18th Australasian Fluid Mechanics Conference, Launceston, Australia, 2012.
8. S.R. Al-Atresh, A.S. Sharifian and A.P. Wandel," The effect of the width and number of gaps on the characteristics of swirl flow induced natually inside split channel using hot air inlet," International Journal of Materials, Mechanics and Manufacturing, 2 (2014), pp. 339-344.
9. S.V. Patankar, *Numerical heat transfer and fluid flow*, (McGraw-Hill Book Company, New York, 1980).
10. J.V. Akwa, G.A.d.S. Júnior and A.P. Petry, "Discussion on the verification of the overlap ratio influence on performance coefficients of a Savonius wind rotor using computational fluid dynamics," Renewable Energy, 38 (2012), pp. 141–149.
11. E.L. Blades and D.L. Marcum, "A sliding interface method for unsteady unstructured flow simulations," International Journal for Numerical Methods in Fluids, 53 (2007), pp. 507–529.
12. S. Mathur, "Unsteady flow simulations using unstructured sliding meshes," 25th AIAA Fluid Dynamics Conference, Washington, D.C., 1994.
13. K.W. McLaren, "A numerical and experimental study of unsteady loading of high solidity vertical axis wind turbines," Ph.D. thesis, Mechanical Engineering, McMaster University, Hamilton, Ontario, Canada, 2011.
14. ANSYS, *ANSYS CFX-solver modeling guide*, USA, 2010.